



Provided by the author(s) and University of Galway in accordance with publisher policies. Please cite the published version when available.

Title	Finite element prediction of creep-plastic ratchetting and low cycle creep-fatigue for a large SPF tool
Author(s)	Leen, Sean B.
Publication Date	2010-03-03
Publication Information	Deshpande, AA,Leen, SB,Hyde, TH (2010) 'Finite element prediction of creep-plastic ratchetting and low cycle creep-fatigue for a large SPF tool'. Journal Of Materials Engineering And Performance, 19 :452-466.
Publisher	Springer Verlag
Link to publisher's version	http://dx.doi.org/10.1007/s11665-010-9610-8
Item record	http://hdl.handle.net/10379/5410
DOI	http://dx.doi.org/10.1007/s11665-010-9610-8

Downloaded 2023-03-31T19:34:53Z

Some rights reserved. For more information, please see the item record link above.



**Finite element prediction of creep-plastic ratchetting and
low cycle creep-fatigue for a large SPF tool**

Journal:	<i>Journal of Materials Engineering and Performance</i>
Manuscript ID:	JMEP-09-12-1553
Manuscript Type:	Technical Paper
Date Submitted by the Author:	09-Dec-2009
Complete List of Authors:	Hyde, T.H.
Keywords:	Superplastic forming, plastic shakedown, heating-cooling cycles, part-forming cycles, thermo-mechanical fatigue and creep, major cycle, minor cycle

Finite element prediction of creep-plastic ratchetting and low cycle creep-fatigue for a large SPF tool

A.A.Deshpande^{1,a}, S.B. Leen^{1,b}, T.H. Hyde^{1,c}

¹School Mechanical, Materials & Manufacturing Engineering, University of Nottingham,
NG7 2RD, UK

^aepxaad@nottingham.ac.uk

^bs.leen@nottingham.ac.uk

^cthomas.hyde@nottingham.ac.uk

Abstract: Industrial experience shows that large superplastic forming (SPF) tools suffer from distortion due to thermal cycling, which apparently causes high temperature creep and plasticity. In addition to distortion, thermo-mechanical fatigue and fatigue-creep interaction can lead to cracking. The aim of the present work is to predict the life-limiting thermo-mechanical behaviour of a large SPF tool under realistic forming conditions using elastic-plastic-creep FE analyses. Non-linear time-dependent, sequentially coupled FE analyses are performed using temperature dependent monotonic and cyclic material data for a high-nickel, high-chromium tool material, XN40F (40% Ni and 20% Cr). The effect of monotonic and cyclic material data is compared vis-à-vis the anisothermal, elastic-plastic-stress response of the SPF tool. An uncoupled cyclic plasticity-creep material model is employed. Progressive deformation (ratchetting) is predicted locally, transverse to the predominant direction of the creep-fatigue cycling, but at the same spatial location, due to creep and cyclic plasticity, during the so-called minor cycles, which correspond to comparatively small-amplitude temperature changes associated with opening of the press doors during part loading and unloading operation.

Keywords: Superplastic forming, plastic shakedown, heating-cooling cycles, part-forming cycles, thermo-mechanical fatigue and creep, major cycle, minor cycle, creep ratchetting

1. Introduction

Superplastic forming is an important manufacturing process for the aerospace and the automotive industries because of its capability of producing highly complex sheet components in a single operation. The SPF process is generally used to form complex geometry shaped components and requires complex shaped tools. Tools play an important role in the success of any manufacturing process. Superplastic forming tools need to withstand high temperature cyclic loading and steady mechanical loading for extended durations and therefore are manufactured (by casting) from specialized alloys, but at the same time numerous additional geometrical complexities results from weight-saving constraints (due for example to weight limitations in industrial plant related to handling capacities, for example) and ruling section requirements for casting. The cost of tool failure is significant and tool life is an important limiting aspect in the SPF process; the SPF process is a high value-added process, rather than a mass production process.

Comparatively little research as been carried out in the area of thermo mechanical analysis of SPF tools. The group of Bernhart and co-workers at Ecoles des Mines at Albi, e.g. [1, 2], have presented thermo-mechanical FE analyses of a simple

AeroMat 2008

Austin, Texas, June 23 – 26, 2008

1
2
3 axisymmetric cylindrical shaped SPF tool and the effects of residual stress and
4 distortion were investigated. A steady state heat transfer analysis was employed with
5 thermal gradients, using non-isothermal boundary conditions, to drive thermo-
6 mechanical FE analysis with elastic-viscoplastic material behaviour during the
7 forming cycle. The thermo-mechanical fatigue properties were measured through
8 thermo-mechanical fatigue tests and a complex unified elastic-viscoplastic material
9 model has been developed for forging and SPF tool materials. Shang et al [3-5] have
10 studied the thermo mechanical, time dependent, elastic-plastic and creep behaviour of
11 large SPF tools using a sequential, three-dimensional, finite element heat transfer and
12 mechanical stress analysis approach. In the absence of sufficient test data, the
13 measured temperature-dependent monotonic stress-strain data was employed to define
14 an anisothermal, linear kinematic hardening model. Shang [4] characterised high
15 temperature behaviour of the 40%Ni-20% Cr, XN40F die material using isothermal
16 fatigue and creep-fatigue interaction tests at 700°C and 900°C. A creep-fatigue life
17 prediction method using a novel bi-linear strain-range partitioning approach was
18 developed and applied to predict the tool life. Shang et al. [3] used simplified
19 boundary conditions, i.e. contact with the platen was not modelled and the effects of
20 clamping pressure during the forming cycle were not considered. .

21
22 Large SPF tools mainly suffer from distortion due to thermal cycling and high
23 temperature creep [6]. Creep relaxation during forming induces inelastic deformation
24 and distortion of the tool after cooling to the ambient [2]. SPF tool distortion can lead
25 to the forming of inaccurate parts which incurs the expense of repair and replacement
26 of such tools. In addition to distortion, the thermo-mechanical fatigue and fatigue-
27 creep interaction can lead to cracking. Finite element (FE) based simulation of
28 realistic thermo-mechanical conditions is an effective (arguably the only full-field)
29 method for analysing realistic large SPF tool behaviour to predict the complex
30 temperature-stress-strain cycles and hence damage and deformation for distortion
31 assessment and hence distortion control or minimisation.

32
33 All engineering structures subjected to cyclic loading above the first yield load
34 of the structure may fail by different mechanisms such as elastic shakedown, plastic
35 shakedown or ratchetting. In elastic shakedown, a structure shakes down to elastic
36 behaviour after an initial elastic-plastic response and may fail after a finite number of
37 cycles due to high cycle fatigue. Structure behaviour exhibiting stable reverse or
38 alternating plasticity over each cycle is referred to as plastic shakedown. In plastic
39 shakedown, the structure can be expected to fail due to low cycle fatigue.
40 Alternatively, structural behaviour exhibiting an accumulation of (plastic) strain with
41 each loading cycle is referred to as ratchetting and incremental plastic collapse or
42 failure of the structure will occur. At high temperature the viscosity of the material
43 and the time dependence of ratchetting become important and should be addressed for
44 the safety of components [6].

45
46 The present paper is concerned with the finite element prediction of the
47 complex anisothermal, time-dependent, thermo-mechanical behaviour of realistic SPF
48 dies, under complex thermo-mechanical load cycles, corresponding to (i) low-
49 frequency bulk heating and cooling of the die and (ii) higher-frequency localised
50 cooling and heating of the die, associated with blank insertion and part removal. The
51 work is relevant to real industrial problems with distortion of such dies, leading to
52 detrimental cracking and die repair/refurbishment overheads and associated outage.
53 The predictions suggest that SPF dies experience low cycle fatigue, creep-fatigue and
54 high temperature creep-plastic ratchetting and that the so-called minor cycles,
55 corresponding to localised cooling and heating of the dies due to press opening for
56
57
58
59
60

1
2
3 blank insertion and part removal, are particularly detrimental with respect to damage
4 accumulation. In the absence of sufficient test data, initially temperature dependent
5 monotonic stress-strain data is used to define a cyclic stress-strain curve. Following
6 Kapoor [7], who considered ratcheting and fatigue to be independent but competing
7 mechanisms, estimated predictions are provided for the ratcheting and creep-fatigue
8 lives of the die to assess their comparative importance.
9
10

11 **2. Tool geometry and material**

12 The geometry of a realistic SPF tool is shown in Figure 1. Side A is approximately
13 2000 mm long and side B is approximately 800 mm long. The bottom side of the tool
14 has eleven cavities of 100 mm depth, for casting purposes. Figure 1 also shows the
15 forming surface of the tool and other features such as alignment lugs and hangers.
16
17

18 In practice major cracks are typically observed along the top edges of the two
19 longer sides shown in Figure 1 while smaller cracks tend to occur at stress
20 concentration features, such as alignment lugs, hangings and corner cavities.
21

22 The tool is cast from XN40F material which is relatively new in the aerospace
23 industry. The composition of XN40F tool material is given in Table 1 [5] while the
24 thermal properties are given in Table 2 [5]. Thermal properties such as thermal
25 conductivity and specific heat at different temperatures are required to predict the
26 thermal histories of the SPF tool.
27

28 The material data from high temperature tensile tests and cyclic isothermal tests
29 from previous work at the University of Nottingham [5], along with new data
30 presented here, are shown in Tables 3, 4 and 5. The tensile tests were carried out for
31 four different temperatures; 20°C, 500°C, 700°C and 900°C which span the
32 temperature range for the SPF process. The average strain rate applied is $8 \times 10^{-4} \text{ s}^{-1}$.
33 Figure 2 and Table 3 shows the results of monotonic tension tests. The elongation to
34 failure increases significantly with increasing temperature. Brittle fracture occurs
35 below 700°C and ductile fracture occurs at 900°C [5]. Short term tensile tests at lower
36 strain rates of $8 \times 10^{-5} \text{ s}^{-1}$ and $8 \times 10^{-4} \text{ s}^{-1}$ at 900°C were carried out to determine the
37 short term creep properties as shown in Table 4 and Figure 3.
38

39 Cyclic isothermal tests at 20°C, 500°C, 700°C and 900°C for different strain
40 ranges were employed to characterise the temperature dependent cyclic stress-strain
41 behaviour of the XN40F alloy. Lower strain-ranges were employed for the lower
42 temperatures, consistent with anticipated relevant in-situ conditions. Figure 4 shows
43 the cyclic stress-strain curves obtained from the tests the different temperatures. It can
44 be seen that the alloy cyclically hardens at all temperature. The degree of hardening is
45 greater at lower temperatures than at higher temperatures. The lowest hardening
46 observed was at 900°C.
47
48

49 **3. Methodology**

50 **3.1 General**

51 The realistic SPF tool shown in Figure 1 is represented in a geometrically simplified
52 form (see Figure 5) to reduce the computational expense and complexities in the FE
53 model. The main simplifications relate to the omission of local features, such as
54 hangings and alignment lugs, so that the dominant deformation mechanisms are still
55 captured, since the objective here is to address the major cracks observed in real tools.
56 A lower half of the SPF tool is modelled assuming symmetry between the upper and
57 lower tool. The platen-tool contact is defined as a mechanical boundary condition in
58 the FE model. This representative tool has five cavities of 100 mm depth on the
59 underside of the tool.
60

The transient heat transfer methodology used here is the same as that previously validated against the measured heating and cooling experiments for a model die at the University of Nottingham [4]. A realistic SPF thermal history is modelled in the commercial, general-purpose, non-linear FE code, ABAQUS, using conduction, convection and radiation mechanisms.

3.2 Heat transfer modelling

Thermal conductivity is a thermo physical property of material which is a function of temperature and location, i.e. $k = k(T, x, y, z)$ [8]. In the present work, since the die is assumed to be homogeneous and isotropic, it is assumed to that $k = k(T)$ only. The temperature-dependent conductivity data from Table 2 is employed in the FE modelling of the SPF thermal cycles.

Newton's law of cooling which gives the relation between convective heat transfer rate and temperature difference between the surface T_s and ambient T_∞ is used to model convective heat transfer [8], as follows

$$q'' = h(T_s - T_\infty) \quad (1)$$

where h is the convective heat transfer coefficient and q'' is the convective heat flux. SPF tools are commonly (or at least partially) cooled with a natural flow of air, so that the natural convection mechanism is assumed for calculating convective heat transfer coefficients.

Convective heat transfer coefficients are commonly expressed using the Nusselt non-dimensional number which is defined as

$$Nu_L = \frac{hL}{k} = CRa_L^n \quad (2)$$

where L is the characteristic length of the geometry, k is the conductivity of air, and Ra_L is the Rayleigh number, given by:

$$Ra_L = \frac{g\beta(T_s - T_\infty)L^3}{\nu\alpha} \quad (3)$$

where g is the local acceleration due to gravity, β is the volumetric thermal expansion coefficient, defined as $\beta = \frac{1}{T}$ for an ideal gas, ν is kinematic viscosity (m^2/s), and α is thermal diffusivity (m^2/s). The convective heat transfer coefficient changes depending on the surface orientation.

For a vertical surface, which is parallel with the gravitational vector; the buoyancy force causes fluid motion in the upward or downward direction and the following empirical formula is used to calculate h for vertical surfaces [8]:

$$\overline{Nu}_L = 0.68 + \frac{0.670Ra_L^{1/4}}{[1 + (0.492\alpha/\nu)^{9/16}]^{4/9}} \quad Ra_L \leq 10^9 \quad (4)$$

Alternatively, for a horizontal surface, the buoyancy force is normal to the surface and the recommended correlations [8] for the average Nusselt number are given as follows.

(a) For the upper surface of a heated plate or the lower surface of cooled plate:

$$\overline{Nu}_L = 0.54Ra_L^{1/4} \quad (10^4 \leq Ra_L \leq 10^7) \quad (5)$$

$$\overline{Nu}_L = 0.15Ra_L^{1/3} \quad (10^7 \leq Ra_L \leq 10^{11}) \quad (6)$$

(b) For the lower surface of a heated plate or the upper surface of cooled plate:

$$\overline{Nu}_L = 0.27Ra_L^{1/4} \quad (10^5 \leq Ra_L \leq 10^{10}) \quad (7)$$

1
2
3
4
5
6
7
8
9
10
11
12
13
14
15
16
17
18
19
20
21
22
23
24
25
26
27
28
29
30
31
32
33
34
35
36
37
38
39
40
41
42
43
44
45
46
47
48
49
50
51
52
53
54
55
56
57
58
59
60

These equations are employed to calculate the film coefficients for modelling of convective heat transfer of the SPF die.

The ratio of radiation emitted by a surface to the radiation emitted by a black body is called the emissivity [8]. The emissivity of a black body is assumed to equal 1 and no surface can emit more radiation than a black body. The radiative heat transfer is defined here via the following equation:

$$q = eC_{SB}T^4 \quad (8)$$

where e is the radiation emissivity of the surface, q is the surface emissive power (W/m^2), T is the absolute temperature of the surface and C_{sb} is the Stefan-Boltzmann constant, which is equal to $C_{SB} = 5.67 \times 10^{-8} \text{ W} / \text{m}^2 \text{ K}$.

Previous calibration of the present heat transfer methodology against the measured transient temperature history of a representative tool has shown that a value of $e = 0.9$ is appropriate for accurate prediction of the cooling and heating cycles.

3.3 SPF Thermal cycle

The SPF tool temperature cycling is complex and is therefore idealised here as divided into two types. The two types are (i) lower frequency cycles, referred here as major cycles, broadly associated with heating and cooling from ambient, and (ii) higher frequency cycles, referred to here as minor cycles, which are associated with opening and closing of the press doors for blank inserts and removal of formed parts. In reality these cycles are not easy to standardize since they are not automated and are carried out by manual operation. Therefore there can be significant variations in the time periods, in particular, associated with these idealised cycles. Nonetheless, for the purposes of analyses here, they are idealised as follows.

Major cycle

Step 1: The tool is heated in a pre-heat furnace to 500°C at a controlled rate of $50^\circ\text{C}/\text{hr}$ and then allowed to reach steady state by soaking at 500°C . The heating process is mainly controlled by conduction with the temperature boundary condition applied to the bottom surface of the tool. The open radiation and free convection mechanisms are also applied with an ambient temperature of 500°C during the soak time.

Step 2: The tool is transferred to the SPF press in 3 minutes. During this time-period all external surfaces except the top surface of the tool are exposed to the ambient via open radiation and free convection mechanisms.

Step 3: The tool arrives in the SPF press and is heated to 900°C , again at $50^\circ\text{C}/\text{hr}$, until a uniform temperature is achieved. This process is again controlled through the conductive heating of the tool via temperature control of the bottom surface nodes.

Step 4: The tool is control-cooled to 500°C at $50^\circ\text{C}/\text{hr}$ in the SPF press and then removed from the press to cool to ambient temperature via free convection and open radiation.

These four (major cycle) steps are illustrated in Figure 6. Direct heating and cooling to 500°C in the SPF press is always implemented by controlled temperature variation of the tool bottom surface nodes. The contact with the platen is assumed to be adiabatic.

Minor cycle

Step 1: The SPF press is opened to unload the formed component. This consists of allowing the two longest sides of the tool (facing the press

doors) to cool via free convection and open radiation with the ambient for a period of 5 minutes.

Step 2: The press is closed again and the tool is heated back to 900°C.

Step 3: The press is opened again to load the new blank. This again allows the two longest sides to cool via free convection and open radiation for 5 minutes.

Step 4: The press is closed again and the tool is heated back to 900°C along with the new blank sheet.

Step 5: The tool and the blank temperature is maintained at a constant temperature of 900°C for 7 hours corresponding to the forming cycle of one component.

3.4 Constitutive equations

The material constitutive model employed here is a temperature-dependent, linear kinematic hardening (LKH) model, with uncoupled secondary (Norton) creep during the dwell time at 900°C. The Ziegler kinematic hardening law within ABAQUS [9] is used to simulate the translation of yield surface in the stress space, through the back stress, \mathbf{a} .

The total strain rate is decomposed into elastic and plastic strain rates, as follows:

$$\dot{\boldsymbol{\varepsilon}} = \dot{\boldsymbol{\varepsilon}}^{el} + \dot{\boldsymbol{\varepsilon}}^{pl} \quad (9)$$

with the linear elastic behaviour defined as:

$$\boldsymbol{\sigma} = \mathbf{D}^{el} : \boldsymbol{\varepsilon} \quad (10)$$

where \mathbf{D}^{el} is the material stiffness matrix and the yield surface is defined by:

$$f(\boldsymbol{\sigma} - \mathbf{a}) = \sigma^0 \quad (11)$$

where σ^0 is the size of the yield surface and $f(\boldsymbol{\sigma} - \mathbf{a})$ is the equivalent Mises stress with respect to the back stress \mathbf{a} defined as:

$$f(\boldsymbol{\sigma} - \mathbf{a}) = \sqrt{\frac{3}{2} (\mathbf{S} - \mathbf{a}^{dev}) : (\mathbf{S} - \mathbf{a}^{dev})} \quad (12)$$

where \mathbf{a}^{dev} is the deviatoric part of the back stress and \mathbf{S} is the deviatoric stress tensor. The flow-rule equation is:

$$\dot{\boldsymbol{\varepsilon}}^{pl} = \frac{\partial f(\boldsymbol{\sigma} - \mathbf{a})}{\partial \boldsymbol{\sigma}} \dot{\boldsymbol{\varepsilon}}^{pl} \quad (13)$$

where $\dot{\boldsymbol{\varepsilon}}^{pl}$ is the equivalent plastic strain rate defined as follows:

$$\dot{\boldsymbol{\varepsilon}}^{pl} = \sqrt{\frac{2}{3} \dot{\boldsymbol{\varepsilon}}^{pl} : \dot{\boldsymbol{\varepsilon}}^{pl}} \quad (14)$$

The size of the yield surface $\sigma^0(T)$ is a function of temperature T and the generalised Ziegler's rule for an-isothermal case is given in equation below.

$$\dot{\mathbf{a}} = C \dot{\boldsymbol{\varepsilon}}^{pl} \frac{1}{\sigma^0} (\boldsymbol{\sigma} - \mathbf{a}) + \frac{1}{C} \mathbf{a} \dot{C} \quad (15)$$

where $C(T)$ is the temperature-dependent hardening modulus of the isothermal uniaxial stress-strain response, $\frac{\partial \boldsymbol{\sigma}}{\partial \boldsymbol{\varepsilon}^{pl}}$, measured at different temperatures and \dot{C} is the

1
2
3 rate of change of C with respect to temperature, as given in Tables 3 and 5, for the
4 monotonic and cyclic data respectively.

5
6 A steady state (secondary) creep behaviour is introduced during the (minor
7 cycle) dwell time at the constant temperature of 900°C. Creep is applied in the model
8 using power-law (Norton) creep $\dot{\epsilon}^{cr} = Aq^n t^m$ where A , n and m are temperature
9 dependent material constants, $\dot{\epsilon}^{cr}$ is the uniaxial equivalent creep strain rate, q is the
10 equivalent (von Mises) stress, and t is the total time. A value of $m = 0$ is assumed
11 here, so that only secondary creep is considered.
12
13

14 15 3.4 Finite element modelling

16 Sequentially coupled thermo-mechanical analyses are performed to simulate the
17 thermo-mechanical behaviour of the SPF tool. The time-dependent temperature
18 distribution from the transient heat transfer phase is employed in a subsequent
19 thermo-mechanical analysis, where thermal stresses and strains are calculated using
20 temperature-dependent thermal expansion coefficients. As mentioned above, only the
21 lower half of the tool is modelled, as a first approximation and on the basis of
22 approximate symmetry between the two halves. The presence of upper tool is
23 modelling via the clamping pressure applied along the top edge of the lower tool
24 during the dwell time. The gas pressure during forming is not modelled as the stresses
25 induced by the forming pressure are considered to be negligible [2]. Tool gravity is
26 modelled along with frictional contact between the tool bottom surface and platen.
27
28

29 In FE analysis, contact is classified as a discontinuous constraint which allows
30 forces to be transmitted from one part to another. The constraint is only applied when
31 the two surfaces are in contact and hence the analysis has to be able to detect when the
32 two surfaces are in contact and apply the constraint accordingly. Contact problems are
33 difficult to converge and must be addressed properly. The contact between the two
34 surfaces is defined using the slave-master algorithm in ABAQUS. The platen is
35 defined as an analytically rigid surface and is assigned to be the master surface. The
36 bottom surface of the tool is defined as a slave surface. The platen (master surface) is
37 extended enough well beyond the bottom surface (slave) of the tool to avoid slave
38 surface nodes 'falling off the edge' of the master surface. Interaction between
39 contacting surfaces consist of normal and tangential components. When two surfaces
40 are in contact with each other, the force normal to the contacting surfaces acts on the
41 two bodies. The surfaces separate when contact pressure between them becomes zero
42 or negative and the constraint is removed. This surface interaction is referred to as
43 hard contact [9] and is used to model the normal behaviour between the platen and the
44 tool. In the presence of friction, shear forces are created between the contacting
45 surfaces, which resist the tangential motion of the bodies. The Coulomb friction
46 model is used here to describe this interaction between the platen and the tool. The
47 frictional behaviour is defined using a coefficient of friction μ which is equal to 0.2 in
48 the tool-platen contact. Contact with friction is difficult to converge due to the
49 discontinuity between the two states of sticking or slipping. A penalty friction
50 formulation with an allowable elastic slip is employed here. The allowable elastic slip
51 is the small amount of relative motion that occurs when surfaces should be under
52 sticking state which corresponds to a very small fraction of the characteristic element
53 length [9]. An allowable elastic slip value of 0.2 mm is used here.
54
55

56 First order elements are always preferred for slave surfaces over second order
57 elements [9] and hence 8 noded (linear) brick elements with reduced integration are
58 used in the thermo-mechanical analyses. The ABAQUS algorithm always checks for
59
60

changes in the contact conditions (closed or opened) before checking for equilibrium forces and moments. Iterations with contact state changes detected are called severe discontinuity iterations. In order to converge contact successfully, the maximum number of severe discontinuity equations allowed are changed from default 12 to 30 in the current problem and the contact is converged successfully.

A reference point on the platen is constrained in all six degrees of freedom throughout the analyses. Boundary conditions are applied at nodes A and B (Figure 5) in the beginning of the analysis to restrict tool rotation across the horizontal plane until the friction between the platen and the tool bottom surface is completely active i.e. only during the application of gravity of the tool.

The SPF tool is subjected to three different types of loading during the SPF process, namely thermal-mechanical loading, gravity loading and clamping pressure. Tool gravity is applied at the beginning of the analyses and remains active throughout. The clamping pressure of 4 MPa is applied along the top surface edges of the SPF tool just before the forming cycle and remains active during the 7-hour forming period. The clamping pressure in real dies is commonly actively controlled, both spatially and temporally, but this aspect is not modelled here.

3.5 Tool life prediction methodology

It is well known that some materials, such as stainless steel 304, do not follow a straight-line failure interaction locus [5]. The Ni-Cr alloy of the present work is generically somewhat similar to stainless steel 304, which is sometimes used as a die material for high temperature (900°C) SPF-related processes. Consequently, Shang [5] has proposed a bi-linear creep-fatigue interaction approach for the present XN40F die material.

Shang [5] has shown, from finite element modeling similar to that of the present work, that SPF experience both $\Delta\varepsilon_{pp}$ and $\Delta\varepsilon_{pc}$ cyclic inelastic strain ranges, i.e. cyclic strain ranges with plastic strain reversed by plastic strain ($\Delta\varepsilon_{pp}$) and cyclic strain ranges with plastic strain reversed by creep strain plastic ($\Delta\varepsilon_{pc}$). Associated with these are two damage components, $D_{pc} = \frac{N_f}{N_{pc}}$ and $D_{pp} = \frac{N_f}{N_{pp}}$. The bi-linear damage summation equations, as shown in Figure 8a, are as follows:

$$\frac{N_f}{N_{pp}} + \beta \frac{N_f}{N_{pc}} = 1 \quad \text{for } \frac{N_f}{N_{pc}} < \frac{N_f}{N_{pp}} \quad (16)$$

$$\alpha \frac{N_f}{N_{pp}} + \frac{N_f}{N_{pc}} = 1 \quad \text{for } \frac{N_f}{N_{pp}} < \frac{N_f}{N_{pc}} \quad (17)$$

where N_{pp} is the number of cycles of $\Delta\varepsilon_{pp}$ to failure and N_{pc} is the number of cycles of $\Delta\varepsilon_{pc}$ to failure and where α and β are constants, both greater than 1.

These equations can be further expanded using Miner's rule to linearly combine major and minor cycle damage, as follows:

$$N_f \left[\left(\frac{1}{N_{pp}^{maj}} + \frac{2n}{N_{pp}^{min}} \right) + \beta \left(\frac{1}{N_{pc}^{maj}} + \frac{n}{N_{pc}^{min}} \right) \right] = 1 \quad (18)$$

$$N_f \left[\alpha \left(\frac{1}{N_{pp}^{maj}} + \frac{2n}{N_{pp}^{min}} \right) + \left(\frac{1}{N_{pc}^{maj}} + \frac{n}{N_{pc}^{min}} \right) \right] = 1 \quad (19)$$

where n is the number of minor cycles in a major cycle. A typical value of $n = 20$, which is representative of industrial practice for the present application, is considered here for predicting the number of major cycles. The total number of minor cycles is $2n$ to take into account the fact that the press doors are opened and closed separately for blank sheet loading and part unloading operations.

Strain controlled fatigue and fatigue-creep interaction tests on XN40F material were carried out at 700°C and 900°C by Shang [5] and the resulting cyclic strain-life equations at 900°C are employed here in the bilinear strain-range partitioning approach, as follows:

$$N_{pp}(\Delta\varepsilon_{pp})^{1.346} = 1.745 \quad (20)$$

$$N_{pc}(\Delta\varepsilon_{pc})^{1.518} = 0.462 \quad (21)$$

Additional tests at 900°C, specially devised to simulate the interaction between $\Delta\varepsilon_{pp}$ and $\Delta\varepsilon_{pc}$ strain ranges for the die, were employed by Shang [5], to show that

$\frac{N_f}{N_{pp}} < \frac{N_f}{N_{pc}}$ for the die material and to identify the relevant value of α for Equation

17, as shown in Figure 8b. The resulting average value of $\alpha = 4.53$ is employed here.

As shown in the results section below, the SPF die exhibits a ratchetting phenomenon, in addition to the creep-fatigue cyclic behaviour addressed via the latter bilinear strain-range partitioning approach. The significance of this ratchetting behaviour is assessed here via a simple life (crack initiation) prediction approach, based on the work of Kapoor [7], whereby failure is assumed to occur when the accumulated strain due to ratchetting reaches the uniaxial failure strain (ductility), i.e. a ductility exhaustion approach. Thus, the predicted number of cycles to ratchetting failure, N_r^f , defined here as the occurrence of ductility exhaustion over a volume of approximately 25 mm (typical element size at ratchetting location, with one integration point per element) is given by:

$$N_r^f = \left(\frac{\varepsilon_f}{n\Delta\varepsilon_{eq}^r} \right) \quad (22)$$

where ε_f is the ductility, as determined from tensile tests, and $\Delta\varepsilon_{eq}^r$ is an equivalent ratchet strain, defined as in a manner akin to the definition of equivalent plastic strain, as follows:

$$\Delta\varepsilon_{eq}^r = \left(\sqrt{\frac{2}{3} \left(\Delta\varepsilon_{ij}^r \Delta\varepsilon_{ij}^r \right)} \right) \quad (23)$$

where $\Delta\varepsilon_{ij}^r$ are the tensorial ratchet strain components, calculated from the time histories of each individual strain component, as follows:

$$\Delta\varepsilon_{ij}^r(k) = \varepsilon_{ij}^{in,m}(k) - \varepsilon_{ij}^{in,m}(k-1) \quad (24)$$

where $\varepsilon_{ij}^{in,m}(k)$ is the mean inelastic strain corresponding to the k^{th} minor cycle since, as shown below, the ratchetting phenomenon is associated with the minor cycle creep-plastic deformation. Equation 23 is applied to each minor cycle to obtain a $\Delta\varepsilon_{eq}^r$ value for each minor cycle and an average $\Delta\varepsilon_{eq}^r$ value over all of minor cycles is then employed in Equation 22.

4. Results

4.1 Thermal results

Figure 9a shows the effect of opening and closing of the press doors on the temperature distribution in the die. Clearly, a significant thermal gradient develops between points adjacent to the front and back doors, e.g. EL C in Figure 9a, and points away from the doors, e.g. EL D in Figure 9a. Figure 9b shows the FE-predicted temperature histories of EL C and EL D, illustrating in particular the significant thermal gradient of approximately 150°C during the opening of the press doors (for five minor cycles). The major cycle heating is controlled according to recommendations from SPF die manufacturers to a maximum rate of 50°C/hr, which the present and previous analyses, e.g. [5], show is satisfactory with respect to prevent plasticity occurring. Previous work by the authors [11] has similarly shown that controlled cooling to 500°C prevents plasticity, as compared to free cooling to ambient from 900°C. These controls are therefore employed in the SPF process. However, control of the minor cycle heating and cooling rates (or indeed time periods) is unfortunately not so readily achievable.

4.2 Thermo-mechanical results

4.2.1 Monotonic material data

Figure 10 shows the FE-predicted accumulated equivalent plastic strain at the end of three major cycles, each including five minor cycles. Clearly, plasticity is predicted to occur along the top interface edges of the two sides of the tool facing the press doors. As shown in Figure 9, the temperature drops along these edges during part loading and unloading, leading to large temperature gradients. A local co-ordinate system is defined in Figure 10 where the X direction (also referred to as 1 direction) is parallel to the edge of the tool on which EL C is present and the Y -direction (also referred to as 2-direction) is parallel to the thickness of the tool. Figure 11 shows the predicted von-Mises stress history during the first major cycle for EL C. The predicted maximum von Mises stress of 118 MPa occurs during the part loading and unloading operation, when the temperature drops down to 744°C along the top interface edges of the two sides of the tool facing the press doors, leading to plasticity deformation, as shown in Figure 12a, due to the thermal stresses exceeding the temperature dependent yield stress. In fact, the plastic deformation occurs while the temperature is dropping to 744°C. The von Mises stress is seen to relax from 107 MPa to 8 MPa during the dwell time at 900°C, due to creep deformation. The constant clamping pressure of 4 MPa across the edges of the top four sides of the tool is also introduced during the dwell time at 900°C.

Figure 12a shows the predicted local σ_{11} stress versus inelastic strain, ε_{11}^i for EL C for three major cycles, including the associated minor cycles. Plastic shakedown is predicted to occur for this combination of stress-strain components, which essentially represents the normal stress-inelastic strain response parallel to the side of the long side of the die. This suggests that low cycle fatigue is a likely failure mode in this direction.

To understand the minor cycle, anisothermal stress-strain response, the local stress-strain response is plotted for the first minor cycle of the first major cycle in Figure 12b, for EL C. Thus, this point is predicted to experience compressive stresses during the heating-up process to 900°C, because it is on the surface and heats up faster than the rest of the die. No plasticity is predicted to occur during this period which comprises slow heating up to 500°C in the pre-heat oven, tool transfer from the

1
2
3 preheat oven to the SPF press and slow heating up to 900°C in the SPF press. During
4 tool transfer from the pre-heat oven to the SPF press, tensile stress is predicted due to
5 the bottom surface cooling faster than the top surface, which is modelled as being in
6 contact with the upper half of the tool (via an adiabatic boundary condition).
7

8 During part loading and unloading, a tensile stress is predicted due to the
9 temperature dropping to 744°C, the bulk of the tool (i.e. away from the doors)
10 remaining at 900°C. Elastic recovery followed by compressive plastic strain is
11 predicted during re-heat back to 900°C after every (minor cycle) part load and unload
12 operation. Compressive creep is predicted to follow the compressive plasticity during
13 the dwell time while the stress relaxation is predicted due to creep. Hence, the
14 analyses predict low cycle fatigue and fatigue-creep interaction damage. Figure 12b
15 also shows the inelastic strain ranges $\Delta\varepsilon_{pp}^{maj}$, $\Delta\varepsilon_{pp}^{min}$ and $\Delta\varepsilon_{pc}^{min}$.
16
17

18 In addition to the cyclic plasticity and plasticity reversed by creep cycles, a
19 progressive ratchetting phenomenon is also predicted along the top edges of the tool.
20 This phenomenon results from the fact that the creep strain accrued during the dwell
21 time of the minor cycles exceeds the the plastic deformation accrued (due to thermal
22 gradients) during the part loading and unloading processes. This phenomenon is
23 illustrated via the results of Figures 13 and 14, for EL C. Figure 13a shows the
24 predicted evolutions of local inelastic strains, ε_{22}^{in} and ε_{33}^{in} , corresponding to the Y
25 and Z directions (see Figure 10 for axes definition) with time, including three major
26 cycles, each with five minor cycles, while Figure 13b shows the corresponding
27 temperature-strain responses. These plots clearly illustrate the progressive strain
28 accumulation. Tensile ratchetting strain is predicted for the Z-direction while
29 compressive ratchetting strain is predicted for the Y-direction (vertical), leading to an
30 effectively shear-driven ratchetting process (the local strain components correspond to
31 principal strain directions), where the shear is approximately transverse to the X-
32 direction and the shear strain is approximately equal in magnitude to the average of
33 ε_{22}^{in} and ε_{33}^{in} . Figure 13b shows that the predicted ratchetting is restricted to the
34 approximate temperature range of 744°C to 900°C. Figure 14 shows the evolution of
35 the mean local inelastic strains, $\varepsilon_{22,m}^{in}$ and $\varepsilon_{33,m}^{in}$, with number of minor cycles, for
36 an analysis of a major cycle which includes 40 minor cycles. Tensile incremental
37 growth is predicted in the Z-direction with approximately 0.5% inelastic strain
38 accumulated over the 40 minor cycles, while compressive incremental deformation is
39 predicted in the Y-direction with approximately 0.58% inelastic strain accumulated
40 over the 40 minor cycles. No ratchetting is predicted in the X-direction.
41
42
43
44
45
46
47
48

49 4.2.2 Cyclic material data

50 Figures 15 to 18 shows the corresponding results from the corresponding analyses
51 using the cyclic material data. It should be pointed out that the material testing
52 indicated that, in general, only about ten to twenty cycles were required for cyclic
53 stress-strain stabilisation. Attention is focussed again on EL C, which is the predicted
54 critical location again, as shown in Figure 15. Figure 16 shows that the von Mises
55 stress history for the first major cycle is akin to that with the monotonic data; one key
56 difference is that the predicted peak stresses are higher than for the monotonic case
57 due to the cyclic hardening behaviour of the material. Figure 17a shows the predicted
58 local $\sigma_{11}-\varepsilon_{11}^{in}$ response, for three major cycles, each including five minor cycles. In
59 comparison with Figure 12 (monotonic case), and apparently due to the cyclic
60

AeroMat 2008

Austin, Texas, June 23 – 26, 2008

hardening slopes being significantly higher than the monotonic values, there is a progressive hardening of the material from minor cycle to minor cycle and from major cycle to major cycle, leading to an increasing mean tensile σ_{11} stress. Figure 17b shows the predicted local $\sigma_{11} - \varepsilon_{11}^{in}$ loop for one major cycle (including only one minor cycle) and, in particular, illustrates that elastic shakedown is predicted after the part load operation as the maximum stress predicted during heating back to 900°C and the subsequent part unload operation is lower than the temperature dependent yield stress. This will also contribute to the cyclic hardening behaviour of Figure 16a, since there will be no Bauschinger effect to kinematically shift the yield surfaces back in the compressive direction if compressive yield does not occur. This is almost the reverse of the phenomenon of mean stress relaxation: the mean σ_{11} stress is increasing. The $\Delta\varepsilon_{pp}^{\min}$ minor cycle strain range is thus zero. Figure 18 shows the predicted evolutions of local inelastic strains, ε_{22}^{in} and ε_{33}^{in} with time, including three major cycles, each with five minor cycles. Again, the trends are akin to those of the monotonic data case, except that the magnitude of the strain accumulation is less, due to the cyclic hardening effects. Figure 19 shows the predicted evolutions of mean inelastic strains with minor cycles for the cyclic data case for a major cycle analysis with 40 minor cycles. Although the general trends are similar to the monotonic data case (cf. Figure 14), the key differences are (i) that the total accumulated strains are lower and (ii) the rates of ratchetting are decreasing at a faster rate. This phenomenon is called finite ratchetting [12]. Plastic shakedown is predicted to occur after initial finite ratchetting in the X-direction. In contrast to the monotonic results, Figure 17a shows that compressive plastic strain is predicted to occur during the 2nd and 3rd major cycles, during heating in the pre-heat oven (from 280°C to 463°C) and during controlled cooling from 900°C to 501°C (see Figure 17a).

4.3 Tool life predictions

Tables 6 and 7 summarise the creep-fatigue life predictions from the bi-linear strain range partitioning method and the ratchetting crack initiation lives, respectively. For the latter, since the ratchetting is accumulated between about 740°C and 900°C, it is not clear which temperature the isothermal ductility data should correspond to. Furthermore, each major cycle is assumed to have twenty minor cycles, corresponding to twenty formed parts per forming campaign, which is typical of industrial practice for the present die, based partly on recent findings by Deshpande et al. [11]. Clearly, increasing the number of parts formed per campaign, will proportionally reduce the predicted number of major cycles to ratchetting crack initiation and have a similar effect on creep-fatigue life. The predicted creep-fatigue life using the cyclic data is much higher than using the monotonic data, mainly due to the elastic shakedown predicted during part unload and heating back to 900°C for the cyclic data case. The average equivalent ratchet strain $\Delta\varepsilon_r^{eq}$ over 40 minor cycles (cf. Figures 14 and 19) is considered for the ratchet life prediction.

5. Discussion

The life limiting phenomena such as ratchetting and fatigue due to cyclic loading generally occur simultaneously in the low cycle fatigue regime. This paper has shown that creep-plastic ratchetting is predicted to occur also in SPF dies under realistic

1
2
3 thermal and mechanical loading histories, in addition to the previously presented
4 (predicted) phenomenon of creep-fatigue damage. These phenomena are considered to
5 be independent here and the SPF tool life is predicted separately based on these
6 individual mechanisms. A number of assumptions were made which can be improved
7 upon in future work, as follows:
8

- 9
10 • A realistic but idealised thermal and mechanical loading history for industrial
11 SPF dies is modelled here. Further work should study the effects of variations
12 in key variables, such as duration for loading and unloading the forming
13 medium, more complex variations (temporal and spatial) in clamping load,
14 incorporation of the effects of the forming cycle proper, the effect of the upper
15 die, platen deformation effects. A simplified SPF tool is modelled and
16 complex geometry features such as alignment lugs, forming surface corners
17 and hangers are excluded. Clearly, these could be expected to have a
18 significant effect on predicted life, particularly if located at the co-location of
19 creep-fatigue damage and ratchetting damage.
20
- 21 • The predicted ratchetting phenomenon is predicted in the plane transverse to
22 the predominant creep-fatigue direction. Consequently, some type of
23 multiaxial interaction is likely. Thus, the ratchetting process may accelerate
24 damage accumulation by void growth, for example, and this may further
25 exacerbate the creep-fatigue process, leading to significantly shorter lives even
26 than those predicted.
27
- 28 • Although the material model employed was temperature-dependent and
29 incorporated rate-independent plasticity with kinematic hardening effects and
30 uncoupled creep, more complex material models are available, e.g. unified
31 cyclic viscoplasticity models with combined non-linear kinematic hardening
32 and isotropic hardening, so that cyclic stabilisation can also be modelled. The
33 attraction of the present process is the ease with which the required material
34 constants can be obtained.
35

36
37 The predicted SPF tool behaviour and predicted tool life are consistent with industrial
38 observations. Thus, for example, since most XN40F tools are used for less than about
39 100 major cycles, cracking is not generally a problem, but there have been notable
40 and costly exceptions to this; also, the present work is more generally concerned with
41 the development of pragmatic lifing methodologies for advising industrial practice
42 with respect to die operation. However, die refurbishment is a continual problem, with
43 persistent interruptions to die and press operation required for re-machining to
44 maintain tolerances on formed parts. The immediate onset of progressive deformation,
45 see also [11], shows how this can occur.
46
47

48 **6. Conclusion**

49
50 A finite element methodology for predicting the cyclic thermo-mechanical behaviour
51 of a representative large SPF tool under simplified but realistic thermal and
52 mechanical loading histories is studied. The high temperature (isothermal) monotonic
53 and cyclic stress-strain behaviour of the die material, XN40F, is presented. Some key
54 conclusions from the work are as follows:
55

- 56 • Plastic strain is predicted along the exposed sides (top edges) of the die during
57 opening of the press. This strain is predominantly in the direction parallel to
58 these sides.
- 59 • Ratchetting is predicted at the same general locations of the dies, i.e. top edges
60 of exposed sides during press opening, but the ratchetting direction is in the
transverse plane to the exposed sides.

AeroMat 2008

Austin, Texas, June 23 – 26, 2008

- Crack initiation predictions for the ratchetting phenomenon, based on uniaxial ductility exhaustion, give shorter lives than the creep-fatigue prediction methodology, which is based on a bi-linear strain-range partitioning method to combine creep and fatigue damage.
- It is shown that using monotonic data instead of cyclic data predicts shorter creep-fatigue and ratchetting lives, due to cyclic hardening of the die material. Predicted lives ranged between approximately 50 and 1000 cycles. These are broadly consistent with industrial die performance.

Acknowledgements

The authors wish to thank Ian Leaver and John Chippendale of BAE Systems, Salmesbury for helpful discussions. The first author would also like to thank BAE Systems for funding.

References

1. Bernhart, G., Nazaret, F., Martinier, A., Gao, C., Garriga-Majo, D., Cutard, T., and Lours, P., Design of SPF dies based on advanced material behaviour models, *Materials Science Forum* , **447-448** ,2004, 123-130.
2. Gao, C.Y., Lours, P., Bernhart, G. Thermomechanical stress analysis of superplastic forming tools, *Journal of Materials Processing Technology*, **169**, 2005, 281-291.
3. Shang, J., Leen, S.B, and Hyde, T.H., Finite element based methodology for predicting the thermomechanical behaviour of superplastic forming tools. *Proc. IMechE, Part L: J. Materials: Design and Applications*, 2006, **220(L3)**, 113-123.
4. Shang, J., Leen, S.B, and Hyde, T.H., Finite element based life prediction for high temperature cyclic loading of a large superplastic forming die, *J. Strain Analysis*, Vol. 41, no.8. 2006, 539-559.
5. Shang, J. *Thermo-mechanical life assessment of superplastic forming tools*, PhD Thesis, University of Nottingham, September 2005.
6. Kang, G. and Q. Kan, Constitutive modelling for uniaxial time-dependent ratchetting of SS304 stainless steel, *Mechanics of Materials*, 2007, **39(5)**: 488-499.
7. Kapoor, A., A re-evaluation of the life to rupture of ductile metals by cyclic plastic strain, *Fatigue & Fracture of Engineering Materials and Structures*, **17** (2), 1994, p 201–219.
8. Bejan, A, *Heat Transfer*, John Wiley and Sons, 1993.
9. ABAQUS User and Theory Manuals, Version 6.5, HKS Inc., Rhode Is., US, 2004
10. Kraus, H. *Creep Analysis*, 1980 (John Wiley, Chichester).
11. Deshpande, A.A., Leen, S. B. and Hyde, T. H., Finite element based predictions of life limiting behaviour for a large SPF tool, *Materialwissenschaft und Werkstofftechnik*, **39(4-5)**, 2008, 309-316
12. Hübel, H., Basic conditions for material and structural ratchetting, *Nuclear Engineering and Design*, **162(1)**, 1996, p 55-65.

AeroMat 2008

Austin, Texas, June 23 – 26, 2008

Table 1. Composition of the SPF tool material XN40F [5]

Elements	C	Ni	Cr	Fe
Weight %	0.35	40.0	20.0	Balance

Table 2. Thermal properties of XN40F material at different temperatures (after [5]).

Thermal conductivity		Thermal expansion		Specific heat	
λ		α		c_p	
Temperature °C	W/m/K	Temperature °C	$\times 10^{-6}/^\circ\text{C}$	Temperature °C	J/kg/K
20	11	20-100		0	437
500	20	20-500	15.8	500	536
850	26	20-850	17.35	850	603
950	28	20-950	17.7	950	618

Table 3. Measured mechanical properties of XN40F material at different temperatures of strain rate $8 \times 10^{-4}/\text{s}$ [5].

Temperature °C	Young's modulus GPa	0.2% Yield strength MPa	UTS MPa	Elongation (%)	$C = \frac{\partial \sigma}{\partial \bar{\epsilon}^{pl}}$ MPa
20	110	172	332	3	6154
500	108	145	320	6	3182
700	104	110	286	16	1213
900	92	107	120	37	36

Table 4. Measured creep properties of XN40F material of 900°C [5].

Strain rates 1/s	stress MPa	A $\text{MPa}^{-n}\text{s}^{-1}$	n
8×10^{-4}	136	9.14×10^{-14}	4.66
8×10^{-5}	83		

Table 5. Measured mechanical properties of XN40F material at different temperatures from strain controlled cyclic tests ([5] and present work).

Temperature °C	Young's modulus GPa	Yield strength MPa	Peak stress MPa	$C = \frac{\partial \sigma}{\partial \bar{\epsilon}^{pl}}$ MPa
20	110	238	292	16363
500	108	180	292	33939
700	104	175	295	10619
900	92	112	186	6352

AeroMat 2008

Austin, Texas, June 23 – 26, 2008

Table 6. Predicted fatigue-creep life (major cycles) with bi-linear strain range partitioning approach.

	Monotonic data	Cyclic data
$\alpha = 4.53$	178	765

Table 7. Predicted ratchetting lives, N_r^f .

Parameter	Monotonic data	Cyclic data
$\Delta\varepsilon_r^{eq}$ average	0.015%	0.0044%
ε_f @ 900°C	123	420
ε_f @ 700°C	53	182

For Peer Review

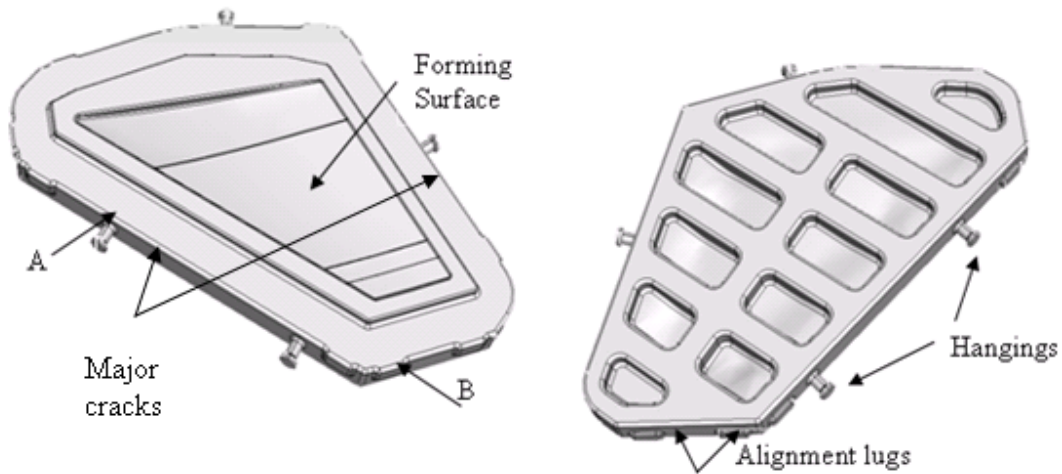


Figure 1. Geometry of realistic superplastic forming tool: (a) top view SPF tool (b) bottom view of SPF tool.

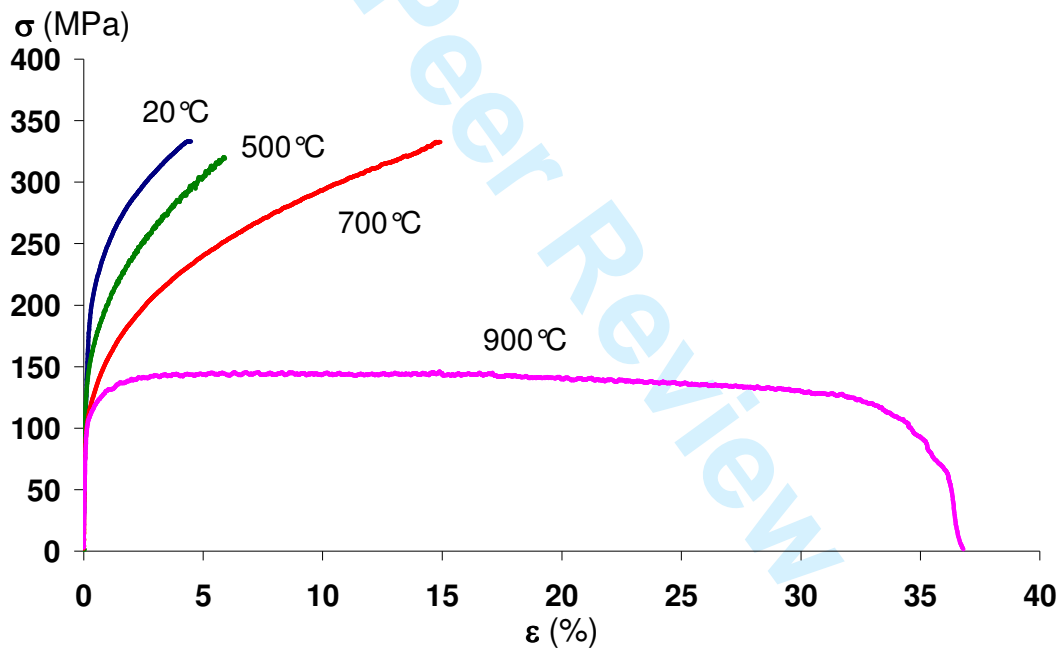


Figure 2. Tensile test stress-strain curves at different temperatures (20°C, 500°C, 700°C and 900°C) for strain rate of 8×10^{-4} /s. [5]

AeroMat 2008

Austin, Texas, June 23 – 26, 2008

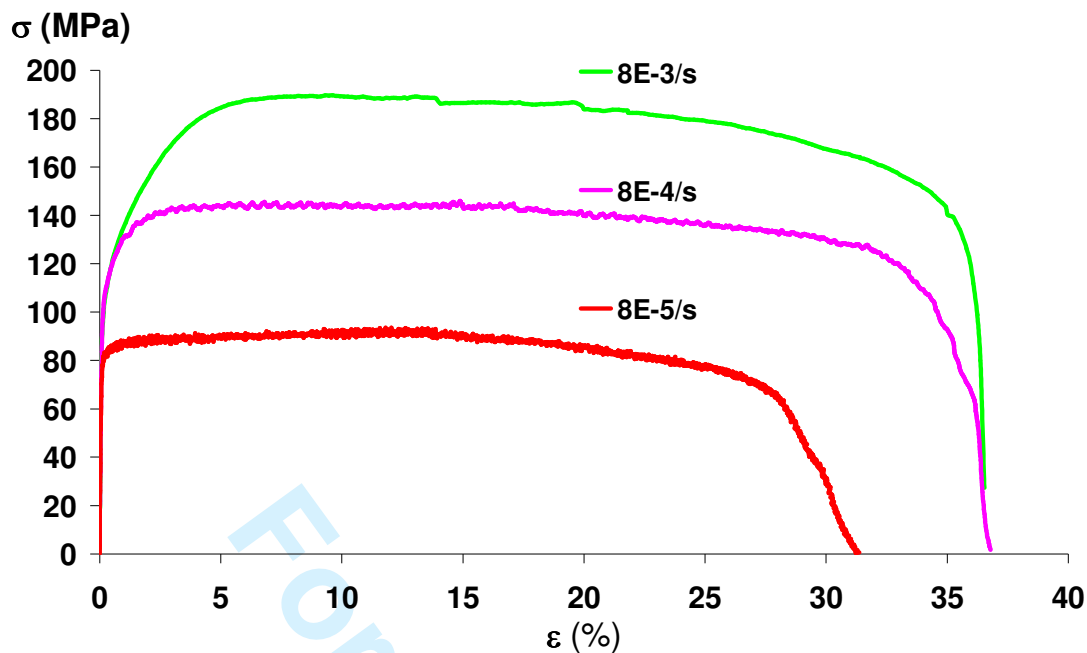


Figure 3. Stress-strain curves of 900°C tensile tests at different strain rates [5].

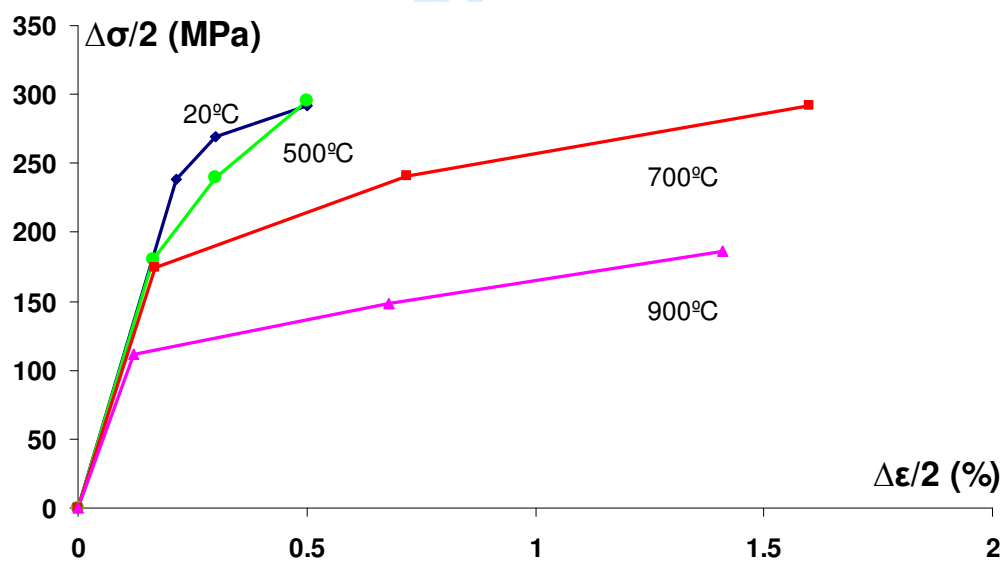


Figure 4. Cyclic test stress-strain curves at different temperatures (20°C, 500°C, 700°C and 900°C) for strain rate of $8 \times 10^{-4}/s$.

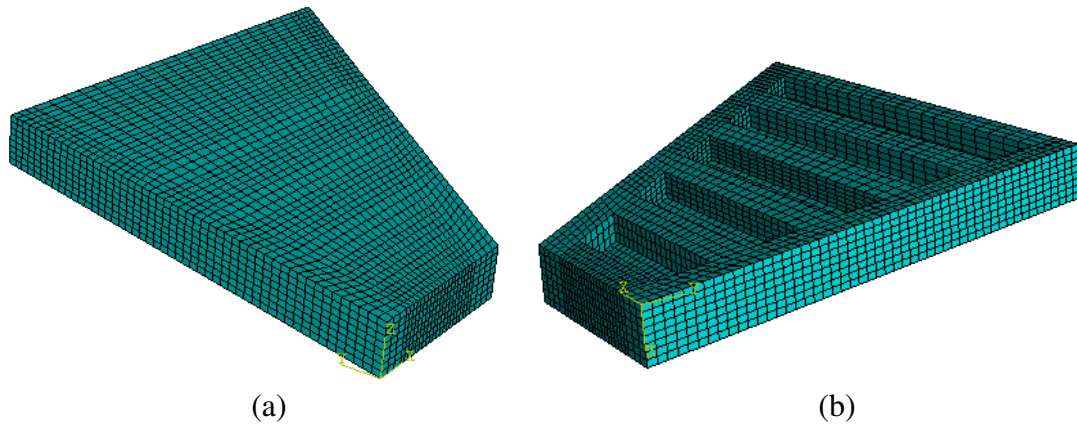


Figure 5. The FE model of a half of a simplified SPF tool: (a) top view, (b) bottom view.

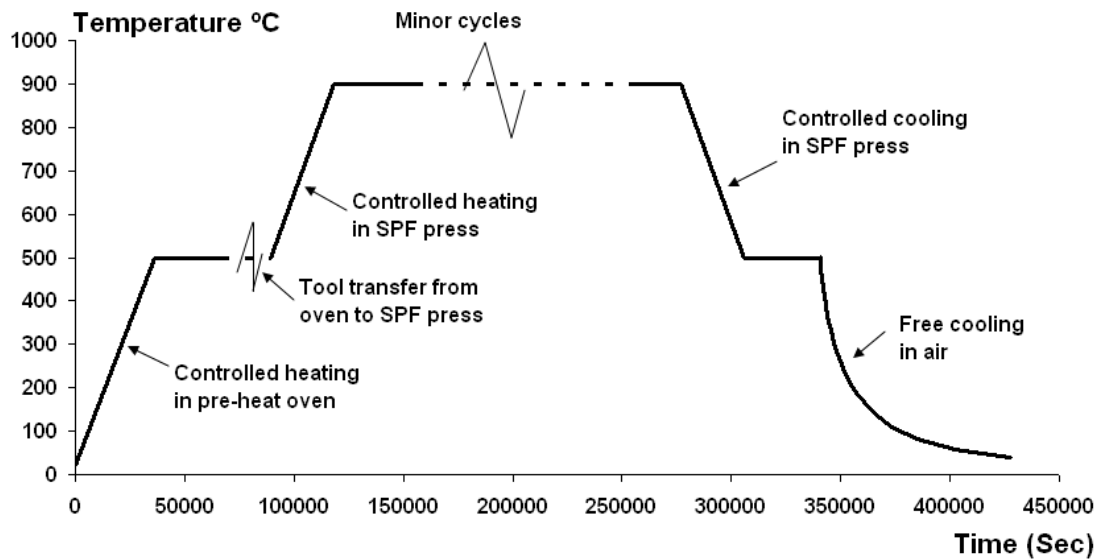


Figure 6. Specified major cycle temperature history of the SPF tool.

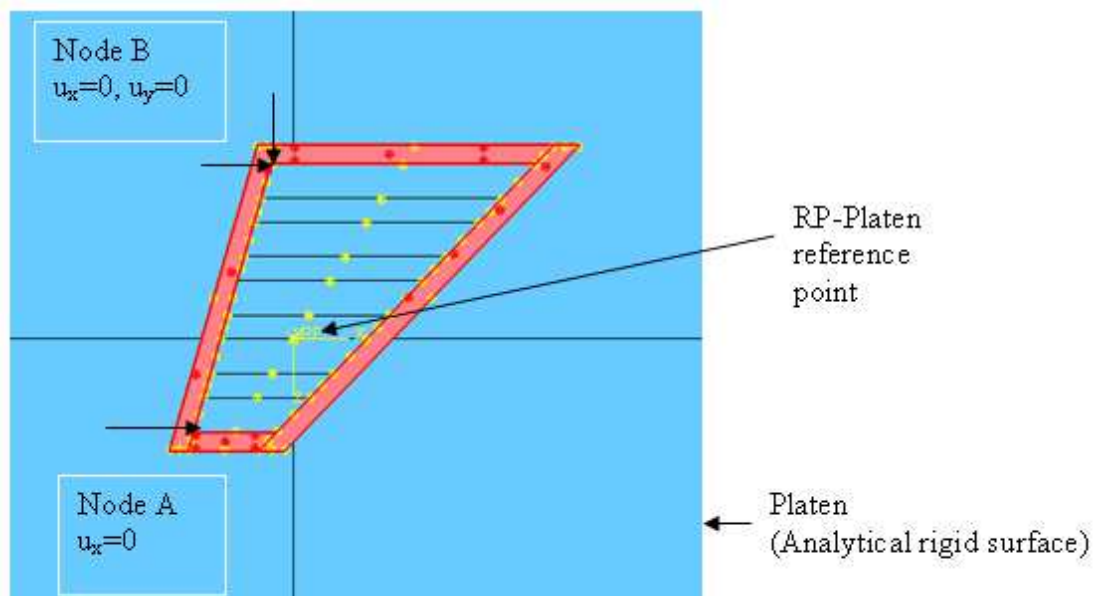
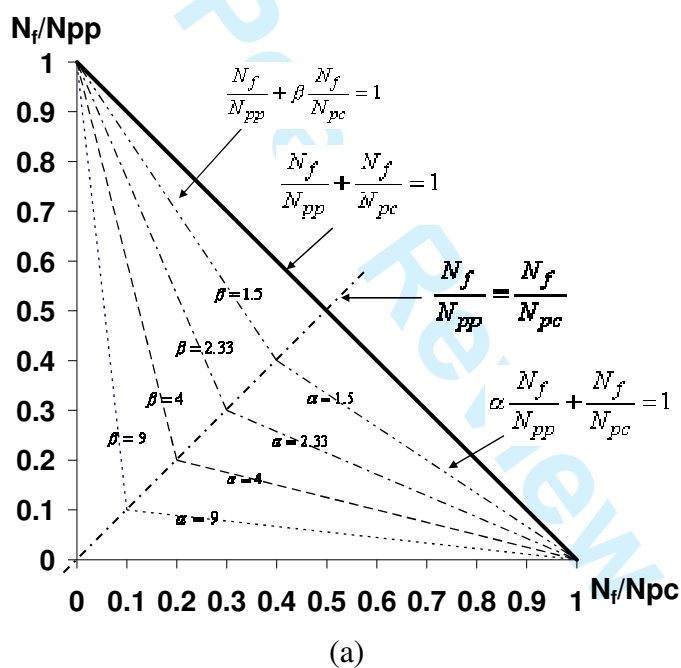


Figure 7. Mechanical boundary conditions and clamping pressure for FE model of SPF tool and platen.



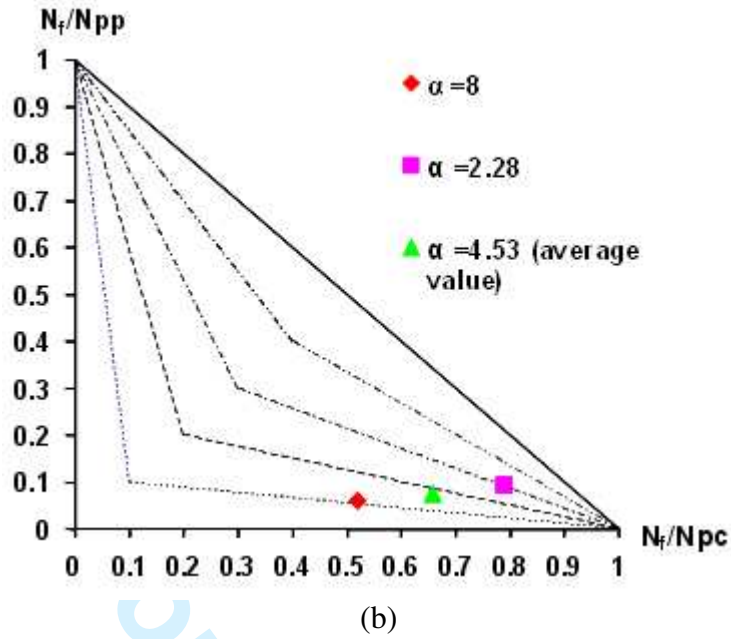
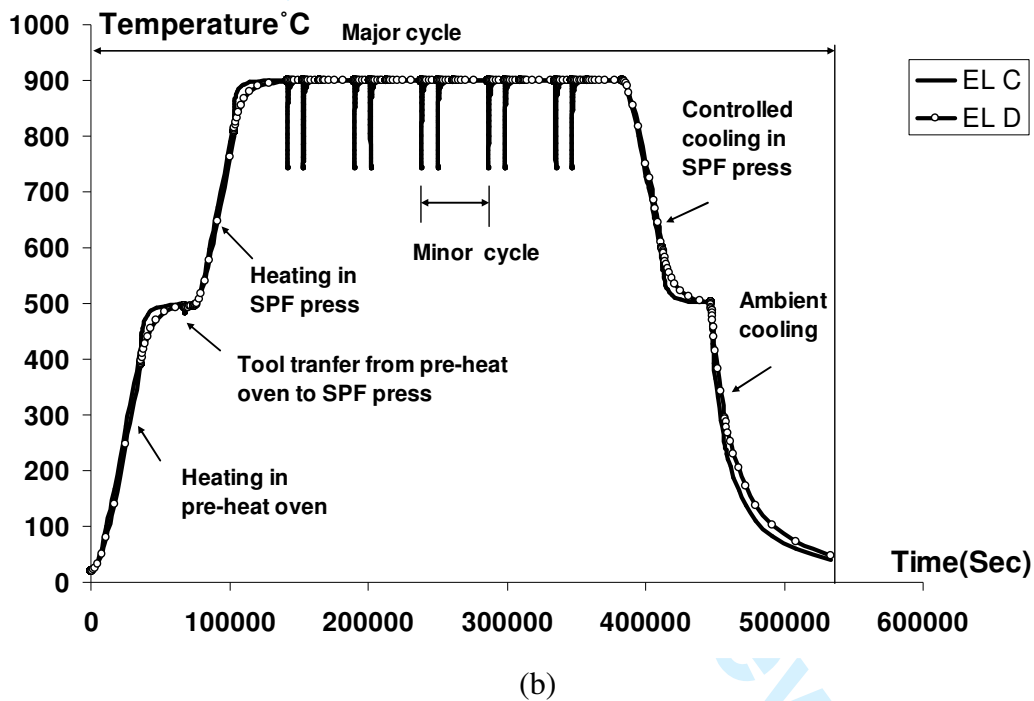
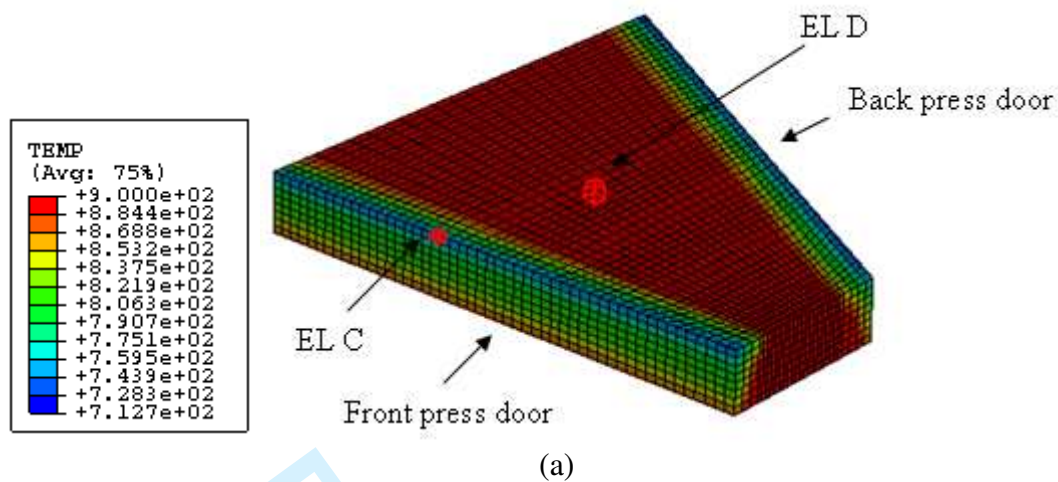


Figure 8. Bi-linear strain range partitioning: (a) schematic plot of the bi-linear damage assumption approach and (b) measured α values from combined creep-fatigue tests on the schematic creep-fatigue interaction diagram [2-4].

AeroMat 2008

Austin, Texas, June 23 – 26, 2008



45
46
47
48
49
50
51
52
53
54
55
56
57
58
59
60

Figure 9. (a) FE-predicted temperature contour plot at the end of part loading and unloading (minor cycle) and (b) temperature histories for sample elements, EL C and EL D.

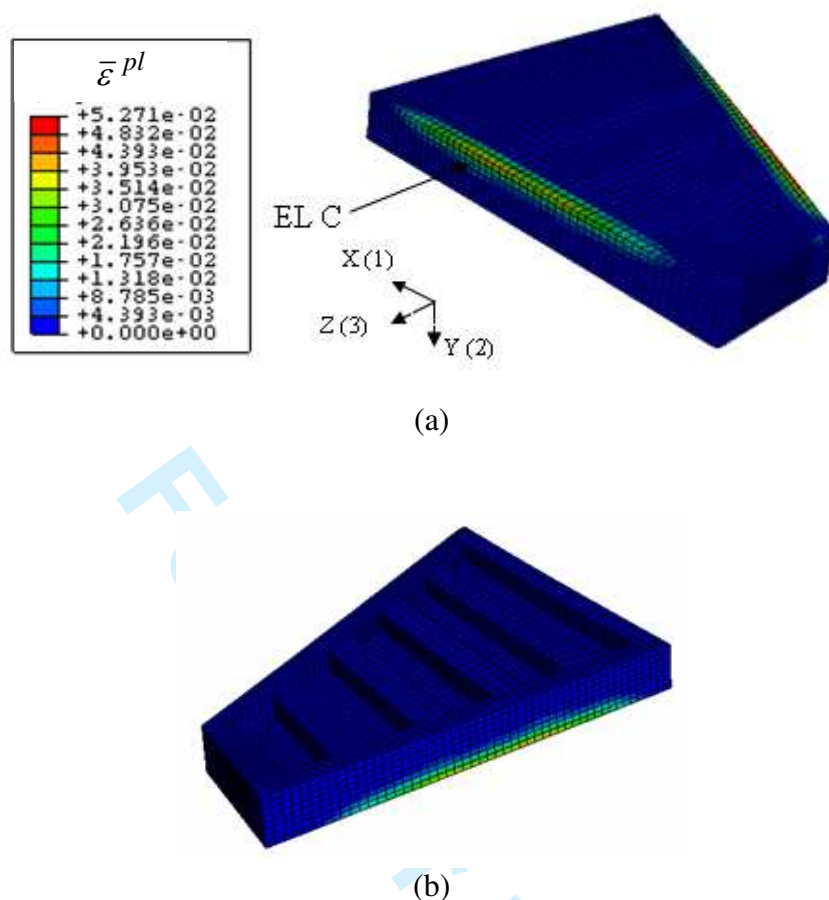


Figure 10. Equivalent plastic strain distribution at end of 3rd major cycle (monotonic material data) for (a) overhead view of die and (b) underside view of die.

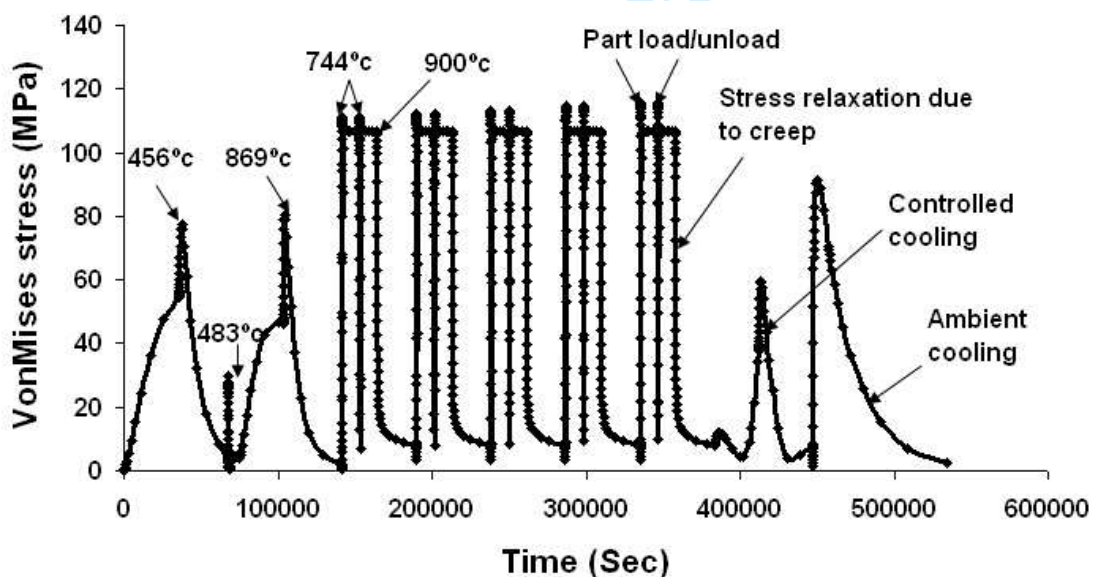
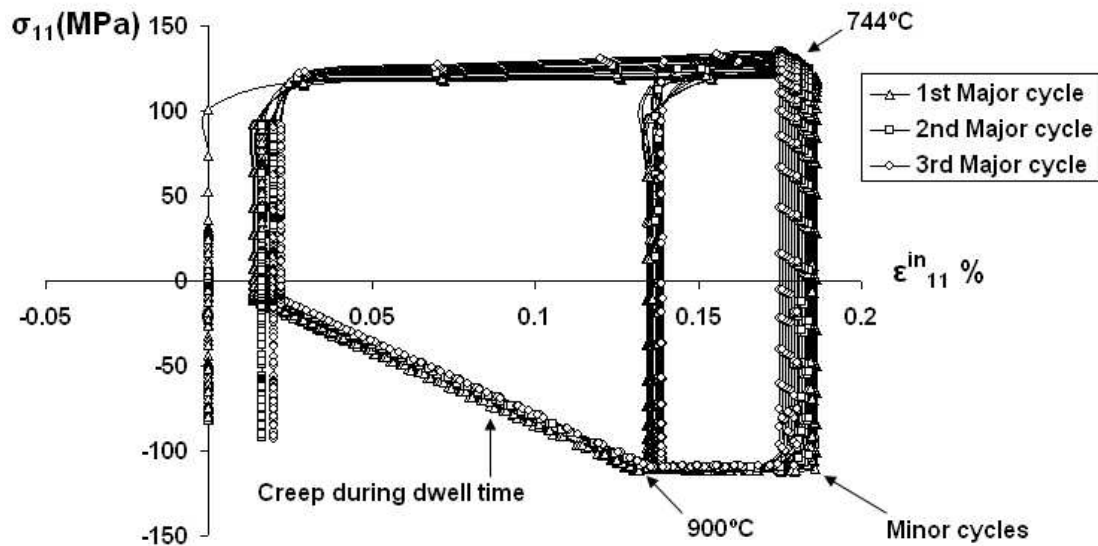


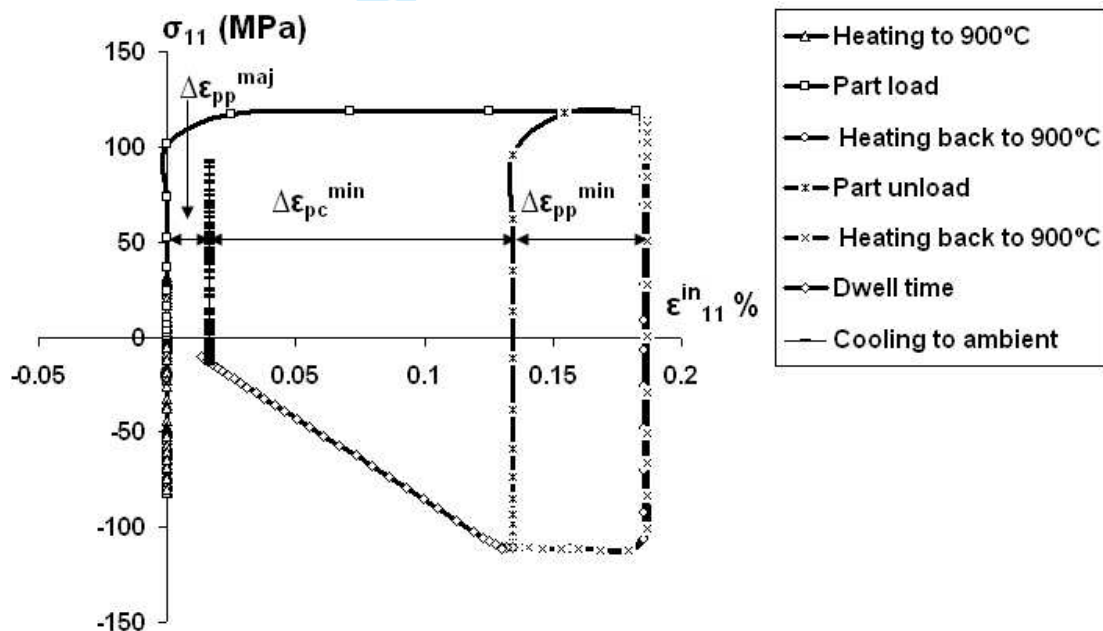
Figure 11. Predicted von Mises stress history for the first major cycle which includes five minor cycles with monotonic material data.

AeroMat 2008

Austin, Texas, June 23 – 26, 2008

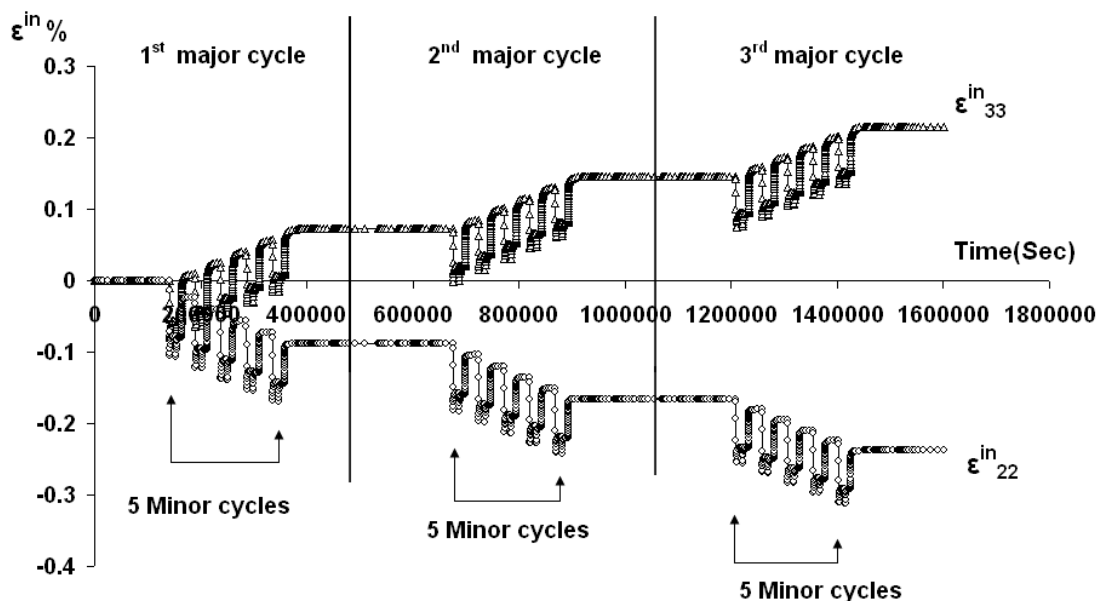


(a)

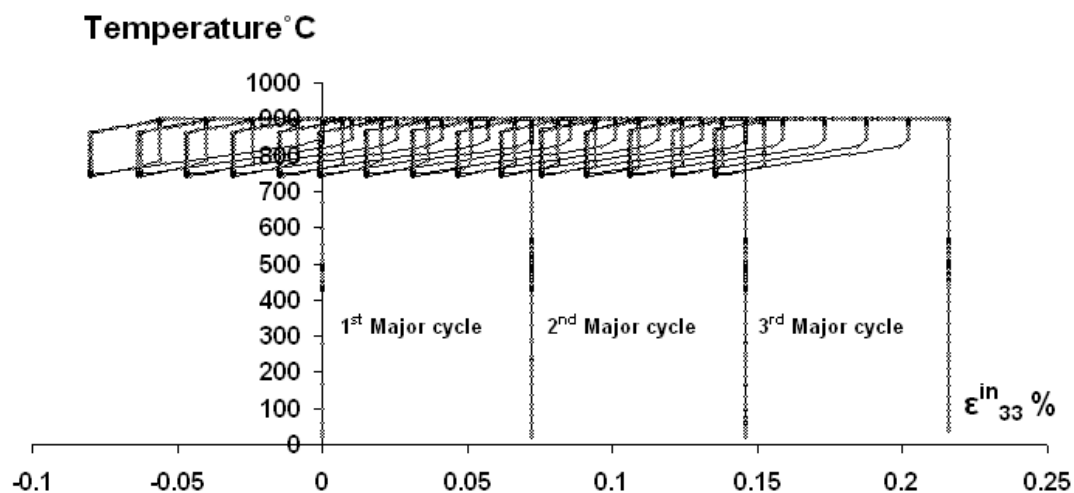


(b)

Figure 12. Local stress versus local inelastic strain (a) for 3 major cycles each include 5 minor cycles with monotonic material data; (b) for the 1st minor cycle of the 1st major cycle with monotonic material data



(a)



(b)

Figure 13. (a) Predicted time histories of local inelastic strains (ϵ^{in}_{22} and ϵ^{in}_{33}) and (b) Temperature versus ϵ^{in}_{33} local inelastic strain, over the duration of three major cycles, each including five minor cycles (monotonic material data).

AeroMat 2008

Austin, Texas, June 23 – 26, 2008

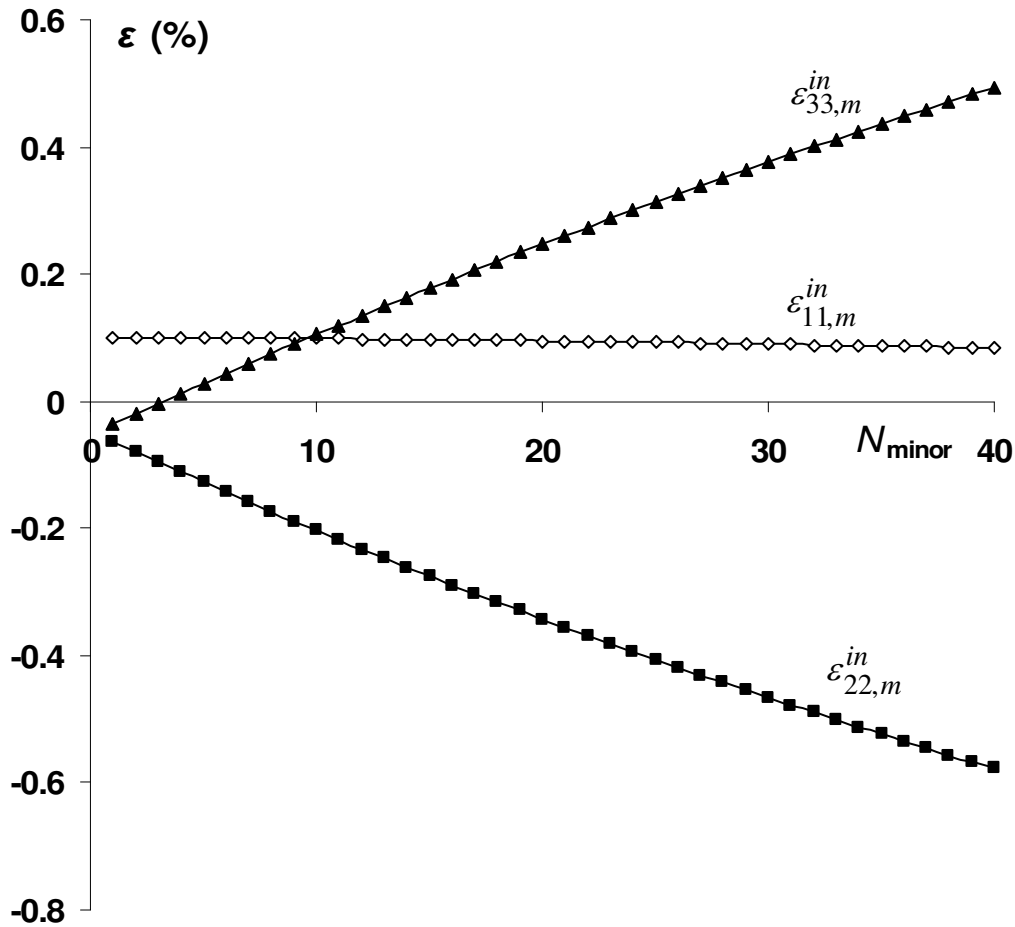


Figure 14. Predicted evolution of inelastic mean strain with minor cycles (monotonic material data) over one major cycle with 40 minor cycles.

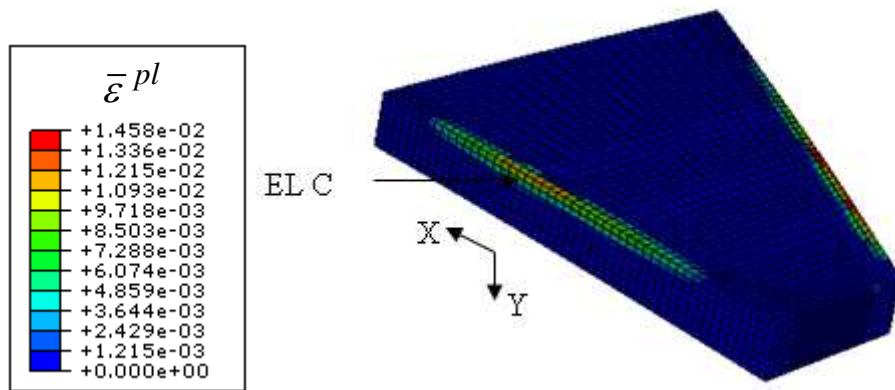


Figure 15. Equivalent plastic strain distribution at end of 3rd major cycle with cyclic material data.

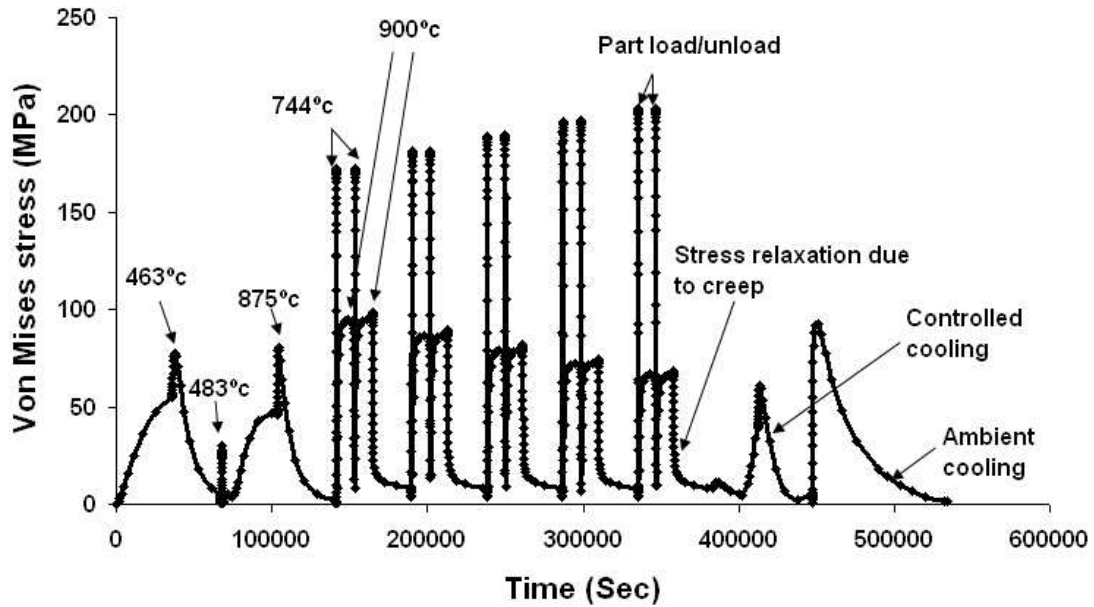


Figure 16. Predicted von Mises stress history for the 1st major cycle which includes five minor cycles with cyclic material data.

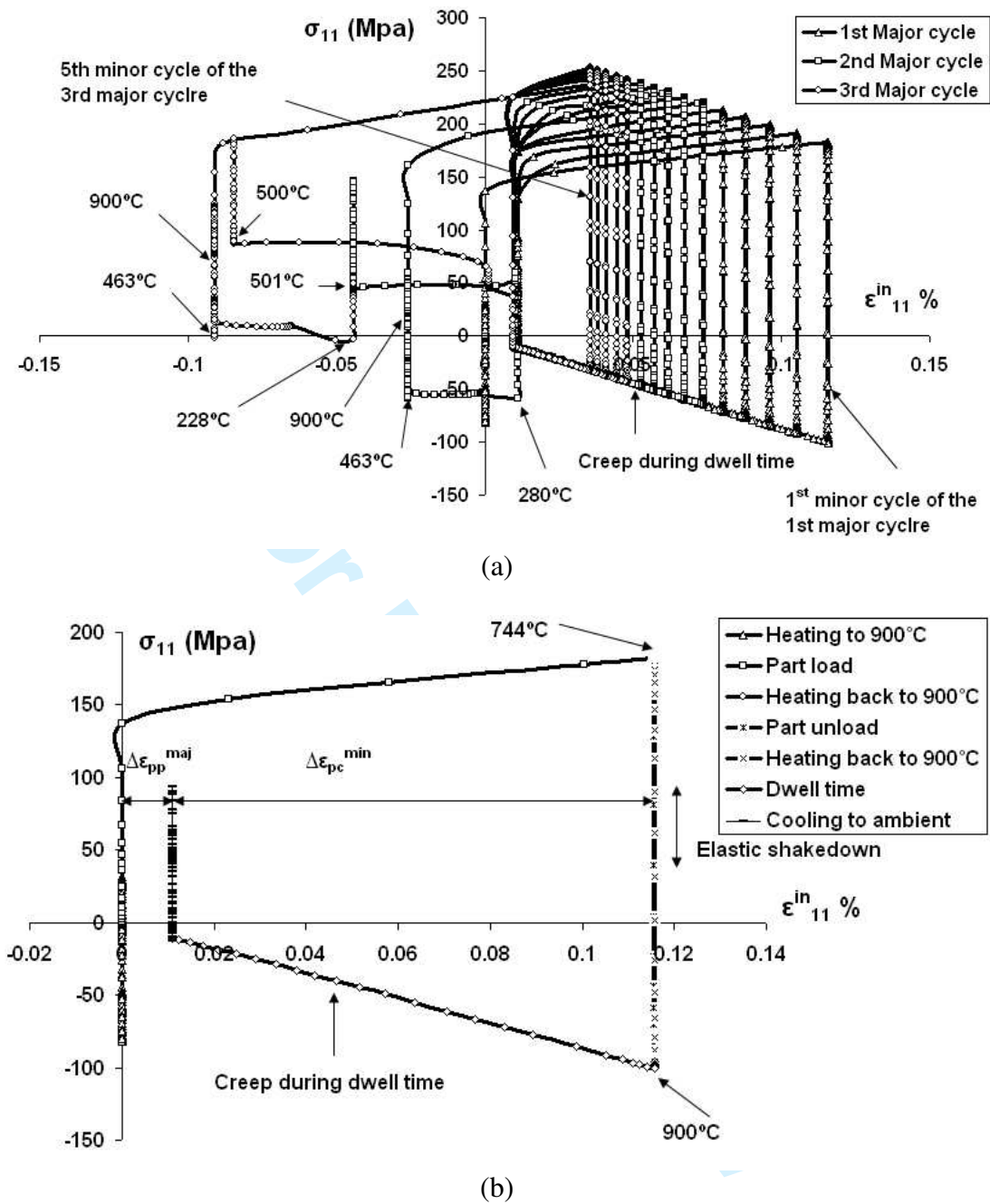


Figure 17. Local stress versus local inelastic strain (with cyclic material data): (a) for the 1st minor cycle of the 1st major cycle; (b) for the 1st minor cycle of the 1st major cycle.

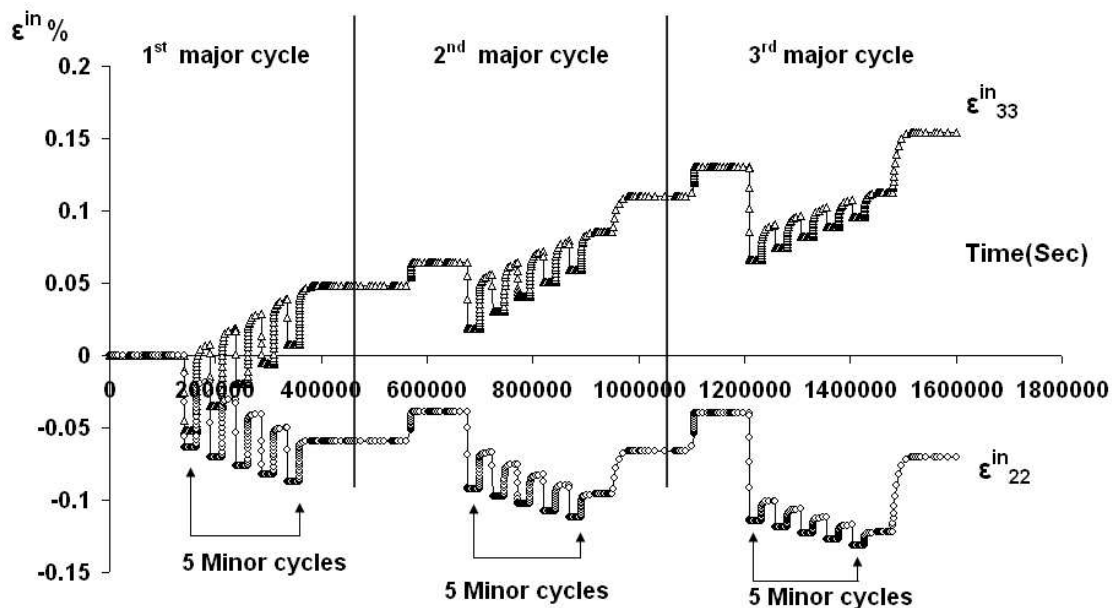


Figure 18. Local inelastic strains (ϵ^{in}_{22} and ϵ^{in}_{33}) history for three major cycles each including five minor cycles (cyclic material data).

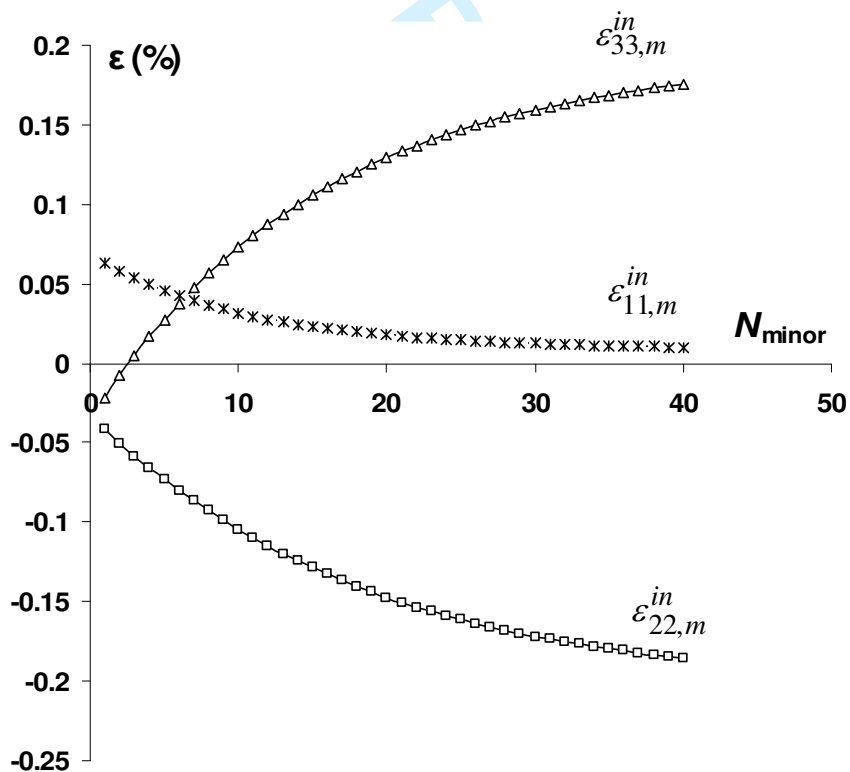


Figure 19. Local inelastic mean strains versus number of minor cycles (cyclic material data).